Conditions for perfect circular polarization of high-order harmonics driven by bichromatic counter-rotating laser fields

John Heslar, Dmitry A. Telnov, and Shih-I Chu

Phys. Rev. A **99**, 023419 — Published 15 February 2019

DOI: 10.1103/PhysRevA.99.023419

Conditions for perfect circular polarization of high-order harmonics driven by bichromatic counter-rotating laser fields

John Heslar,[1] Dmitry A. Telnov,[2,*] and Shih-I Chu[1,3,†]

[1] *Center for Quantum Science and Engineering, and Center for Advanced Study in Theoretical Sciences, Department of Physics, National Taiwan University, Taipei 10617, Taiwan*

[2] *Department of Physics, St. Petersburg State University, 7-9 Universitetskaya nab., St. Petersburg 199034, Russia*

[3] *Department of Chemistry, University of Kansas, Lawrence, Kansas 66045, USA*

Recently, studies of high-order harmonic generation (HHG) from atoms driven by bichromatic counter-rotating circularly polarized laser fields have received considerable attention for this process could be a potential source of coherent circularly polarized extreme ultraviolet (XUV) and soft-x-ray beams in a tabletop-scale setup. In this paper, we address the problem with molecular targets and perform a detailed quantum study of the H_2^+ molecule in bichromatic (ω_0, $2\omega_0$) counter-rotating circular polarized laser fields where we adopt wavelengths (790 and 395 nm) and intensities (2×10^{14} W/cm^2) reported in a recent experiment [K. M. Dorney *et al.*, Phys. Rev. Lett. **119**, 063201 (2017)]. Here, we demonstrate appropriate conditions to produce perfectly circular polarized harmonics. The calculated radiation spectrum contains doublets of left and right circularly polarized harmonics which display perfect circular polarization with use of the trapezoidal pulse shape, and substantial deviations from perfect circular polarization with use of the sine-squared pulse shape. We also study in detail short- and long-cycle counter-rotating circularly polarized driving pulses with a time delay between the two driving fields, ω_0 and $2\omega_0$. These time delayed circularly polarized driving pulses are applied to H atoms and H_2^+ molecules, and in both atomic and molecular cases we conclude a zero time delay corresponds to the highest HHG intensity for short pulses. For longer pulses there are no distinct differences in HHG intensities between the zero and non-zero time delays if the latter are within a few optical cycles of the fundamental frequency.

I. INTRODUCTION

High-order harmonic generation (HHG) is an attractive table-top source of coherent, bright, and tunable extreme ultraviolet (XUV) and soft X-ray radiation with applications in coherent diffractive imaging, ultrafast holography, and time resolved measurements [1–6]. Moreover, circularly polarized HHG may find additional applications in nanolithography, ultrafast spin dynamics, and magnetic circular dichroism [1, 7–16].

However, until recently bright HHG was limited to linear polarization due to the difficulty of controlling elliptically and circularly polarized harmonics and their efficiency. When an atom or molecule is driven by a laser field with slightly elliptical polarization, the electron has some probability of re-colliding with its parent ion it was initially released from, and this results in the generation of harmonics with slight elliptical polarization. A direct approach for generating circularly polarized HHG was suggested 22 years ago [17, 18], and recently measured by Fleischer *et al.* [7]. In this scheme, circularly polarized HHG are driven by co-propagating circularly polarized bichromatic fields that rotate in opposite directions (counter-rotating) and interact with argon gas. This experiment [7] opened up the possibility and motivation of generating bright circularly polarized HHG comparable to the flux efficiency of linearly polarized HHG. Remarkable progress has been achieved recently in the generation and control of the circularly polarized harmonic radiation [1, 7, 12, 14, 19–23].

The primary characteristics of the HHG spectra produced by counter-rotating bichromatic circularly polarized laser fields can be described in terms of the energy and angular momentum conservation, which gives rise to a doublet structure of the HHG spectra. The right peak in the doublet has a circular polarization with the same helicity as the driving field with the higher frequency, the left peak has a circular polarization with the same helicity as the driving field with the lower frequency [1, 7–16, 24]. However, this is a simplified picture based on the assumption that both circularly polarized driving fields are pure monochromatic and the HHG process is not affected by the resonances.

For a more realistic case of pulsed driving fields interacting with atoms or molecules described in full dimensionality, the question about the degree of circular polarization of the harmonics within each doublet still remains open. Barreau *et al.* [14] recently explored the depolarization and ellipticity of high harmonics driven by ultrashort bichromatic circularly polarized fields, and showed deviations from perfect circular polarization. We also partially addressed this problem and uncovered the degree of circular polarization in the harmonic radiation for diatomic molecules subject to bichromatic counter-rotating circularly polarized intense laser fields [15, 16]. Our detailed investigations in Ref. [15] described the distinct differences in the nonlinear optical responses for

* d.telnov@spbu.ru

† sichu@ku.edu

homonuclear (H_2^+ and N_2) and heteronuclear (CO) diatomic molecules subject to circularly polarized intense laser fields. Mainly, for heteronuclear (CO) diatomic molecules where the laser fields are propagated along the molecular (z) axis and circularly polarized on the perpendicular $x-y$ plane causes a nonsymmetric time-dependent displacement of the electron density along the molecular axis thus inducing an oscillating dipole moment in the z direction, although the force from the laser fields does not have a projection on the z axis. Oscillations of the dipole moment along the molecular axis results in the generation of even-order harmonics, linearly polarized in the same z direction. In Ref. [16], we reveal that electron recollisions in molecular systems can be controlled through tailored bichromatic counter-rotating circularly polarized intense laser fields. Also, we show how excited-state resonances alter the ellipticity and phase of the generated harmonic peaks [16].

In this work, we investigate the appropriate conditions to provide perfect circular polarization of the harmonics generated in diatomic molecular targets subject to bichromatic counter-rotating circularly polarized intense laser fields. Our calculations of the HHG spectrum reveal that the doublets of left and right circularly polarized harmonics display perfect circular polarization with the use of the trapezoidal pulse shape, and substantially deviate from perfect circular polarization with the use of the sine-squared pulse shape. We also study in detail short and long counter-rotating circularly polarized pulses with the time delay between the two driving fields with the carrier frequencies ω_0 and $2\omega_0$. These time delayed circularly polarized driving pulses are applied to H atoms and H_2^+ molecules, and in both cases we conclude that the zero time delay results in the highest HHG intensity for short pulses. For longer pulses, we uncover there are no distinct differences in the HHG intensities between the zero and non-zero time delays, if the time delay is within two optical cycles of the fundamental frequency ω_0.

The organization of this paper is as follows. In Sec. II we briefly discuss our theoretical and computational approach for general treatment of the multiphoton dynamics of diatomic molecular systems subject to bichromatic counter-rotating circularly polarized intense laser fields. In Sec. III we study the HHG of H_2^+ molecules driven by different bichromatic (ω_0, $2\omega_0$) counter-rotating circular polarized laser pulse shapes (sine-squared and trapezoidal). The HHG spectra exhibit a distinct doublet structure, and the harmonics within each doublet possess circular polarizations with opposite handedness. We provide a proof and necessary conditions for perfect circular polarization and opposite handedness of the harmonics within the doublets by calculating their ellipticity and phase parameters from the dipole acceleration data for below-, near-, and above-threshold HHG regions. In Sec. IV we investigate HHG by time-delayed few-cycle counter-rotating sine-squared pulses first applied to atoms (H), and then to molecules (H_2^+). We uncover there are no advantages when using non-zero time delays between the counter-rotating fields to increase HHG intensities compared to the zero time delay. Section V contains concluding remarks.

II. THEORY AND NUMERICAL TECHNIQUES

To calculate the HHG spectra, we solve the time-dependent Schrödinger equation for the H_2^+ molecule in the bichromatic counter-rotating circularly polarized laser fields. The initial wave function is an unperturbed eigenfunction of H_2^+. For our calculations, we select the ground ($1\sigma_g$) electronic state. The nuclei are fixed at their positions, and the nuclear motion is not taken into account. To describe the diatomic molecular ion H_2^+, we make use of the prolate spheroidal coordinates ξ, η, and φ which are related to the Cartesian coordinates x, y, and z as follows [25]:

$$\begin{aligned} x &= a\sqrt{(\xi^2-1)(1-\eta^2)}\cos\varphi, \\ y &= a\sqrt{(\xi^2-1)(1-\eta^2)}\sin\varphi, \\ z &= a\xi\eta \quad (1\le\xi<\infty, -1\le\eta\le 1). \end{aligned} \tag{1}$$

In Eq. (1) we assume that the molecular axis is directed along the z axis, and the nuclei are located on this axis at the positions $-a$ and a, so the internuclear separation $R=2a$. The internuclear distance for the H_2^+ ($R_e = 2.00a_0$) molecule is fixed at its equilibrium distance R_e.

A. Generalized pseudospectral method and solution of time-independent eigenvalue problem

First, we solve the unperturbed eigenvalue problem and obtain the eigenvalues and eigenfunctions:

$$\left[-\frac{1}{2}\nabla^2 + U(\xi,\eta)\right]\Psi_n(\xi,\eta,\varphi) = E_n\Psi_n(\xi,\eta,\varphi). \tag{2}$$

Here the kinetic energy operator in the prolate spheroidal coordinates reads as:

$$\begin{aligned} -\frac{1}{2}\nabla^2 = -\frac{1}{2a^2}\frac{1}{(\xi^2-\eta^2)}\Bigg[&\frac{\partial}{\partial\xi}(\xi^2-1)\frac{\partial}{\partial\xi} \\ &+\frac{\partial}{\partial\eta}(1-\eta^2)\frac{\partial}{\partial\eta}+\frac{\xi^2-\eta^2}{(\xi^2-1)(1-\eta^2)}\frac{\partial^2}{\partial\varphi^2}\Bigg], \end{aligned} \tag{3}$$

and the Coulomb interaction with the nuclei is as follows:

$$U(\xi,\eta) = -\frac{(Z_1+Z_2)\xi+(Z_2-Z_1)\eta}{a(\xi^2-\eta^2)}. \tag{4}$$

Here Z_1 and Z_2 are the charges of the left and right nucleus, respectively. For H_2^+, $Z_1 = Z_2 = 1$; for the hydrogen atom, one can choose $Z_1 = 1$ and $Z_2 = 0$. For the unperturbed molecule, the projection m of the angular momentum onto the molecular axis is conserved.

Thus the wave function $\Psi(\xi,\eta,\varphi)$ can be represented in a separable form,

$$\Psi_n(\xi,\eta,\varphi) = \Psi_n^{(m)}(\xi,\eta)\exp(im\varphi), \tag{5}$$

and separate eigenvalues problems for different $|m|$ are obtained,

$$\begin{aligned} &-\frac{1}{2a^2}\frac{1}{(\xi^2-\eta^2)}\left[\frac{\partial}{\partial\xi}(\xi^2-1)\frac{\partial}{\partial\xi}+\frac{\partial}{\partial\eta}(1-\eta^2)\frac{\partial}{\partial\eta}\right.\\ &\left.-\frac{m^2}{\xi^2-1}-\frac{m^2}{1-\eta^2}\right]\Psi_n^{(m)}-\left[\frac{Z_1}{a(\xi+\eta)}+\frac{Z_2}{a(\xi-\eta)}\right]\Psi_n^{(m)}\\ &=E_n^{(m)}\Psi_n^{(m)}. \end{aligned} \tag{6}$$

To solve Eq. (6), we use the generalized pseudospectral (GPS) method. Note that the *exact* eigenfunction ψ_m behaves as $(\xi^2-1)^{|m|/2}(1-\eta^2)^{|m|/2}$ in the vicinity of the nuclei; for odd $|m|$, this is a nonanalytical function of the coordinates. Straightforward numerical differentiation of such a function could result in significant loss of accuracy. We circumvent this difficulty by choosing a special mapping transformation within the GPS method [26]. Other details of the GPS method in prolate spheroidal coordinates can be found in Refs. [15, 16, 27–31].

Solving the eigenvalue problem (6) for different even and odd m, we obtain unperturbed energy values and eigenstates of H_2^+, which are used as initial states for time propagation as well as for construction of propagation matrices.

B. Solution of the time-dependent Schrödinger equation in bichromatic circularly polarized laser pulses

The time-dependent Schrödinger equation in the bichromatic circularly polarized laser pulses is solved by means of the split-operator method in the energy representation [15, 16, 27–32]. We employ the following split-operator, second-order short-time propagation formula:

$$\begin{aligned} \Psi(t+\Delta t) = &\exp\left(-i\frac{1}{2}\Delta t H_0\right)\\ &\times\exp\left[-i\Delta t V_{\rm ext}(\boldsymbol{r},t+\frac{1}{2}\Delta t)\right]\\ &\times\exp\left(-i\frac{1}{2}\Delta t H_0\right)+O((\Delta t)^3). \end{aligned} \tag{7}$$

Here Δt is the time propagation step, H_0 is the unperturbed electronic Hamiltonian which includes the kinetic energy and interaction with the nuclei, $V_{\rm ext}(\boldsymbol{r},t)$ is the term due to the coupling to the bichromatic circularly polarized external fields, in the following form:

$$V_{\rm ext}(\boldsymbol{r},t) = [\boldsymbol{E}_1(t)+\boldsymbol{E}_2(t)]\cdot\boldsymbol{r}. \tag{8}$$

The laser electric-field strengths $\boldsymbol{E}_1(t)$ and $\boldsymbol{E}_2(t)$ refer to the two frequency components of the bichromatic field.

The field-free propagator $\exp(-i\frac{1}{2}\Delta t H_0)$ in Eq. (7) is time-independent; it is calculated only once before the time propagation process begins. The external field propagator $\exp(-i\Delta t V_{\rm ext})$ is time dependent and must be calculated at each time step. However, this operation is not time-consuming, because the external field propagator is diagonal in the coordinate (ξ,η,φ) representation like any multiplication operator in the GPS method.

As a function of the azimuthal angle φ, $\Psi(t)$ can be expanded in Fourier series:

$$\Psi(t) = \sum_{m=-\infty}^{\infty}\exp(im\varphi)\Psi^{(m)}(t). \tag{9}$$

Then the total field-free propagator can be expressed through the propagators corresponding to the specific angular momentum projections [Eqs. (5), (6), and (9)]:

$$\begin{aligned} &\exp\left(-i\frac{1}{2}\Delta t H_0\right)\Psi(t)\\ &\quad=\sum_{m=-\infty}^{\infty}\exp(im\varphi)\exp\left(-i\frac{1}{2}\Delta t H_0^{(m)}\right)\Psi^{(m)}(t). \end{aligned} \tag{10}$$

The partial propagators $\exp(-i\frac{1}{2}\Delta t H_0^{(m)})$ are calculated by the spectral expansion

$$\begin{aligned} &\exp\left(-i\frac{1}{2}\Delta t H_0^{(m)}\right)\\ &\quad=\sum_n\exp\left(-i\frac{1}{2}\Delta t E_n^{(m)}\right)|\Psi_n^{(m)}\rangle\langle\Psi_n^{(m)}|, \end{aligned} \tag{11}$$

where eigenstates $\Psi_n^{(m)}$ and energies $E_n^{(m)}$ are obtained by solving the eigenvalue problem (6) for a real symmetric matrix (upon GPS discretization of $H_0^{(m)}$). Equation (10) is very useful for the calculations where the angular momentum projection is not conserved: in the matrix-vector product, it allows several matrices of a smaller dimension (partial propagators) to be used rather than one matrix of large dimension (full propagator).

Before applying the partial field-free propagators at each time step, the wave function must be converted from the full coordinate representation to the angular momentum projection representation; this is done by the fast Fourier transform (FFT) with respect to the coordinate φ. This operation is performed by the hardware-optimized FFT routines and not time-consuming either.

In what follows, we shall assume that the laser fields $\boldsymbol{E}_1(t)$ and $\boldsymbol{E}_2(t)$ propagate along the z axis and have circular polarizations on the $x-y$ plane. We first consider the sine-squared laser pulse for counter-rotating fields $\boldsymbol{E}_1(t)$ and $\boldsymbol{E}_2(t)$ which has the following form:

$$\boldsymbol{E}_1(t) = \frac{1}{\sqrt{2}}F_0 f(t)\left[\hat{\boldsymbol{e}}_x\cos(\omega_0 t)+\hat{\boldsymbol{e}}_y\sin(\omega_0 t)\right], \tag{12}$$

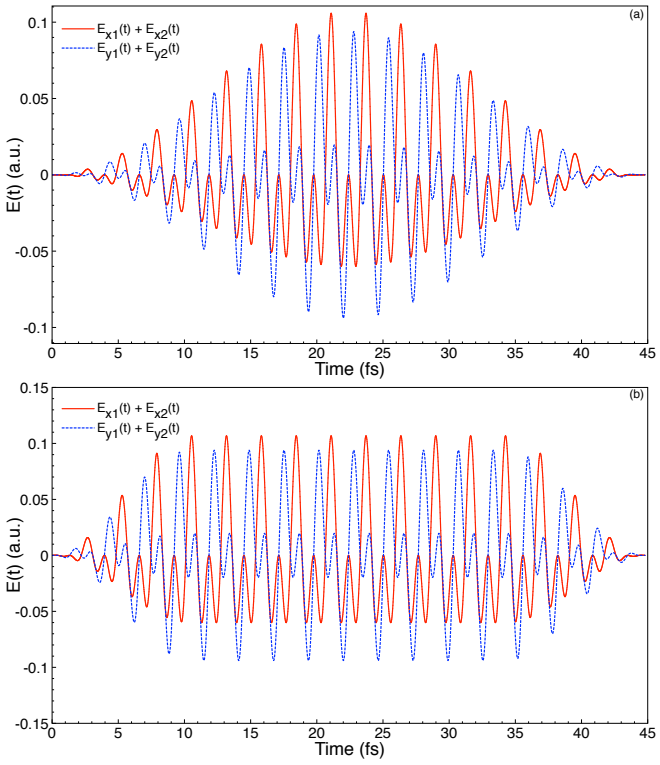

FIG. 1. (Color online) Time-dependent (a) sine-squared and (b) trapezoidal electric field of the driving laser pulse (time-delay $\tau = 0$). The red dotted and blue dashed lines represent the electric field in the x and y direction, respectively. The laser pulses (a) and (b) have a duration of 17 optical cycles ($\sim$ 45 fs) for the ω_0 (790 nm) component and 34 optical cycles ($\sim$ 45 fs) for the $2\omega_0$ (395 nm) component. Both frequency components have the same peak field strength corresponding to the intensity of 2×10^{14} W/cm^2.

$$\boldsymbol{E}_2(t) = \frac{1}{\sqrt{2}} F_0 f(t+\tau) \{\hat{\boldsymbol{e}}_x \cos[2\omega_0(t+\tau)] - \hat{\boldsymbol{e}}_y \sin[2\omega_0(t+\tau)]\}, \tag{13}$$

where τ presents the time delay between the two pulses, $\boldsymbol{E}_1(t)$ and $\boldsymbol{E}_2(t)$. Since the dipole approximation is well justified in the near infrared wavelength region, the fields are assumed uniform in space. In Eqs. (12) and (13), F_0 is the peak electric field strength (we use the same peak field strength for both fields), the carrier frequencies of the first and second fields are ω_0 and $2\omega_0$, respectively, and $f(t)$ represents the temporal pulse envelope,

$$f(t) = \sin^2 \frac{\pi t}{T}, \tag{14}$$

where T is the total pulse duration (again, the same for both fields).

In our calculations, we use the carrier wavelengths 790 nm for the field $\boldsymbol{E}_1(t)$ ($\omega_0 = 0.0576$ a.u.= 1.57 eV) and 395 nm for the field $\boldsymbol{E}_2(t)$ ($2\omega_0 = 0.1152$ a.u.= 3.14 eV), respectively. The peak field strength F_0 corresponds to the intensity 2×10^{14} W/cm^2. The pulse duration is chosen as $T = 34\pi/\omega_0$, that is 17 optical cycles of the field with the wavelength 790 nm or 34 optical cycles of the field with the wavelength 395 nm. One cycle of the ω_0 and $2\omega_0$ fields are 2.64 and 1.32 fs, respectively.

The next pulse envelope shape we consider has a flat top and ramps described by the $\sin^2$ function. The duration of each ramp is equal to 4 optical cycles of the 790 nm field while the duration of the flat central part is equal to 9 optical cycles:

$$f(t) = \begin{cases} \sin^2\left(\dfrac{\omega_0 t}{16}\right), & 0 \le t < \dfrac{8\pi}{\omega_0}; \\ 1, & \dfrac{8\pi}{\omega_0} \le t \le T - \dfrac{8\pi}{\omega_0}; \\ \sin^2\left(\dfrac{\omega_0 (T-t)}{16}\right), & T - \dfrac{8\pi}{\omega_0} < t \le T. \end{cases} \tag{15}$$

In what follows, we shall call the pulse with this envelope the trapezoidal pulse. The total pulse duration for both the sine-squared (14) and trapezoidal (15) envelopes is 45 fs. The circularly polarized laser pulses in the x and y domain (E_x and E_y) are shown in Figs. 1(a) and 1(b) for both the sine-squared (14) and trapezoidal (15) envelope shapes considered.

The dipole interaction potentials in the length gauge have the following expressions in the prolate spheroidal coordinates:

$$\boldsymbol{E}_1(t) \cdot \boldsymbol{r} = \frac{a}{\sqrt{2}} F_0 f(t) \sqrt{(\xi^2-1)(1-\eta^2)} \times \cos(\varphi - \omega_0 t), \tag{16}$$

$$\boldsymbol{E}_2(t) \cdot \boldsymbol{r} = \frac{a}{\sqrt{2}} F_0 f(t+\tau) \sqrt{(\xi^2-1)(1-\eta^2)} \times \cos[\varphi + 2\omega_0 (t+\tau)]. \tag{17}$$

To obtain converged HHG spectra for the laser field parameters used in the calculations, we set the grid size (for ξ, η, and φ coordinates, respectively) to $192 \times 48 \times 48$ and use 4096 time steps per one 395 nm (ω_0) optical cycle in the time propagation process. The spatial and temporal grid parameters have been varied to make sure all the results are fully converged. The linear dimension of the box where the time-dependent equations are solved is chosen as 45 a.u. to ensure accurate description of all important physics for the laser field parameters used in the calculations; between 30 and 45 a.u. we apply an absorber which smoothly brings down the propagated wave functions without spurious reflections from the boundary.

The HHG power spectra can be investigated accurately once the time-dependent wave function $\Psi(\xi, \eta, \varphi, t)$ is available. We calculate the expectation values of the induced dipole acceleration in the x, y, and z directions:

$$a_x(t) = \langle \Psi(\xi,\eta,\varphi,t) | \frac{\partial U(\xi,\eta)}{\partial x} | \Psi(\xi,\eta,\varphi,t) \rangle + E_{1x}(t) + E_{2x}(t), \tag{18}$$

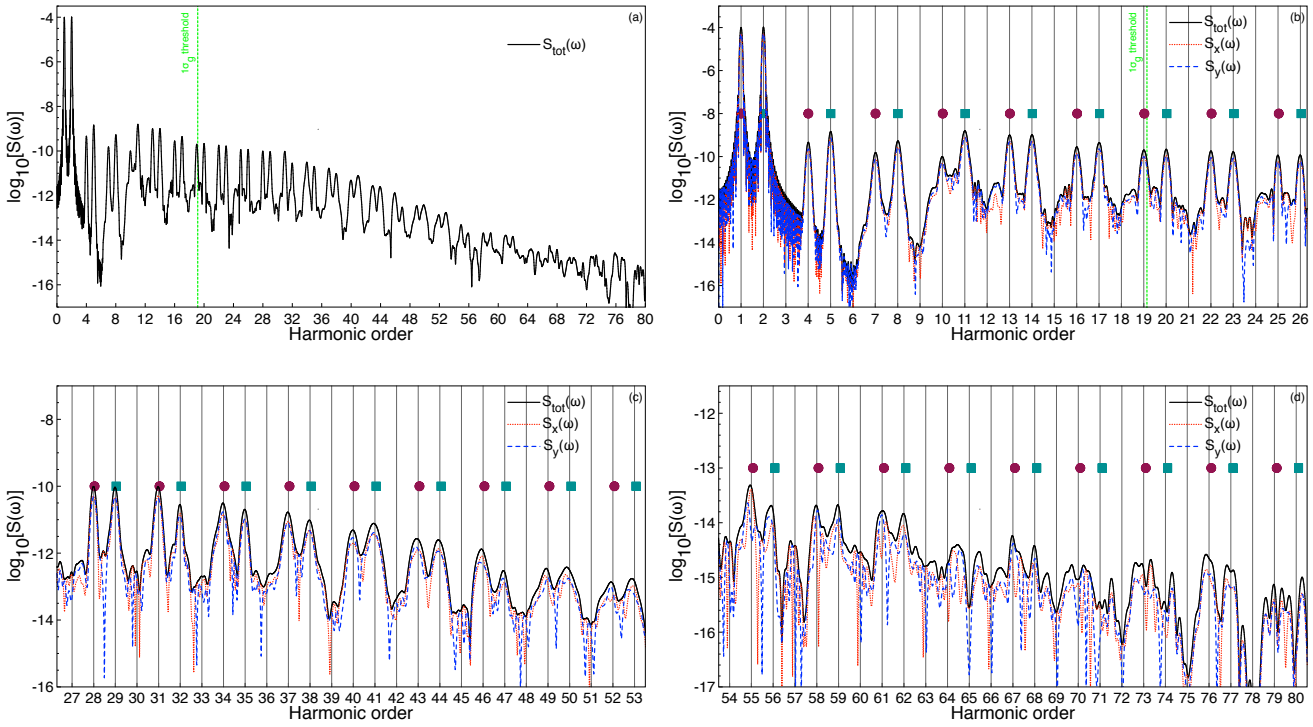

FIG. 2. (Color online) HHG spectrum $S_{\rm tot}(\omega)$ as well as contributions $S_x(\omega)$ and $S_y(\omega)$ from the x and y projections of the dipole acceleration for the H_2^+ molecule subject to the counter-rotating circularly polarized sine-squared laser pulses. Circularly polarized harmonic doublets (a) up to ∼H80, (b) in the below- and near-threshold region (H1-H26), (c) in the above-threshold plateau region (H27-H53), and (d) in the above-threshold plateau and near cutoff region (H54-H80). The laser pulses have a time duration of 17 optical cycles (∼ 45 fs) of frequency ω_0 (wavelength 790 nm) and 34 optical cycles (∼ 45 fs) of frequency $2\omega_0$ (wavelength 395 nm). The black solid, red dotted, and blue dashed lines represent the HHG spectrum in the $S_{\rm tot}(\omega)$, $S_x(\omega)$, and $S_y(\omega)$ domains, respectively. The green vertical dashed line indicates the corresponding ionization threshold (I_p) of the $1\sigma_g$ molecular orbital (H19.13). Filled maroon circles and filled teal squares indicate the positions of the peaks with the frequencies $(3n_c+1)\omega_0$ and $(3n_c+2)\omega_0$, respectively. The separation between the peaks within each doublet is ω_0, and different doublets are separated by $3\omega_0$. Both bichromatic frequency components have the same peak field strength corresponding to the intensity of 2×10^{14} W/cm^2.

$$a_y(t) = \langle\Psi(\xi,\eta,\varphi,t)|\frac{\partial U(\xi,\eta)}{\partial y}|\Psi(\xi,\eta,\varphi,t)\rangle + E_{1y}(t) + E_{2y}(t), \quad (19)$$

$$a_z(t) = \langle\Psi(\xi,\eta,\varphi,t)|\frac{\partial U(\xi,\eta)}{\partial z}|\Psi(\xi,\eta,\varphi,t)\rangle. \quad (20)$$

Then the power spectrum $S(\omega)$ (spectral density of the radiation energy) can be obtained by the Fourier transformation of the time-dependent dipole accelerations,

$$S_x(\omega) = \frac{2}{3\pi c^3}\left|\int_{-\infty}^{\infty} a_x(t)\exp(i\omega t)dt\right|^2, \quad (21)$$

$$S_y(\omega) = \frac{2}{3\pi c^3}\left|\int_{-\infty}^{\infty} a_y(t)\exp(i\omega t)dt\right|^2, \quad (22)$$

$$S_z(\omega) = \frac{2}{3\pi c^3}\left|\int_{-\infty}^{\infty} a_z(t)\exp(i\omega t)dt\right|^2, \quad (23)$$

$$S_{\rm tot}(\omega) = S_x(\omega) + S_y(\omega) + S_z(\omega). \quad (24)$$

We note that for the homonuclear diatomic molecule H_2^+ initially in the state with the definite parity and laser fields polarized in the plane perpendicular to the molecular (z) axis, the contribution $S_z(\omega)$ vanishes.

III. CIRCULARLY POLARIZED HIGH-ORDER HARMONICS, ELLIPTICITY, AND RELATIVE PHASE SHIFT IN H_2^+ MOLECULES

The structure of the HHG spectra can be described in terms of the energy and angular momentum conservation in the process of absorption of the driving

fields photons and emission of the harmonic photon [1, 6, 7, 13, 15–17, 24, 33]. The energy conservation gives $\omega_c = (n_1 + 2n_2)\omega_0$ for the frequency ω_c of the emitted photon after absorption of n_1 photons of frequency ω_0 and n_2 photons of frequency $2\omega_0$. The angular momentum conservation requires $n_2 = n_1 \pm 1$ or $n_2 = n_1$ for the circularly-polarized counter-rotating driving fields $\boldsymbol{E}_1$ and $\boldsymbol{E}_2$. However, for the quantum systems with inversion symmetry such as atoms and homonuclear diatomic molecules, emission of dipole radiation is forbidden in the case $n_2 = n_1$ due to parity restrictions. Then the emitted photon frequency can be represented as $\omega_c = (3n_c + 3/2)\omega_0 \pm \omega_0/2$, n_c being a positive integer number. This gives rise to a doublet structure of the HHG spectrum, with the frequency differences $3\omega_0$ between the adjacent doublets and ω_0 between the photon emission peaks within the same doublet. The right $[(3n_c + 2)\omega_0]$ peak in the doublet has a circular polarization with the same helicity as the driving field with the higher frequency ($\boldsymbol{E}_2$), the left $[(3n_c + 1)\omega_0]$ peak has a circular polarization with the same helicity as the driving field with the lower frequency ($\boldsymbol{E}_1$). The HHG spectrum consists of both odd and even harmonics of the lowest frequency ω_0 except for the harmonic orders that are multiples of 3. In what follows, we will denote the harmonic peaks in the HHG spectrum by their order with respect to the lowest frequency ω_0. We should emphasize that the selection rules and corresponding structure of the HHG spectrum described above are only valid for atoms and homonuclear diatomic molecules when the angular momentum quantization axis can be chosen perpendicular to the polarization plane of the laser fields. For diatomic molecules, it means perpendicular orientation of the molecular axis with respect to the polarization plane. Discussion of other possible situations can be found elsewhere; for example, see Ref. [34] for the case of nonplanar molecules and Ref. [35] for the choice of the quantization axis in the atomic case.

In Figs. 2(a)-(d), we present the HHG spectrum of H_2^+ for the sine-squared (14) driving laser pulse shown in Fig. 1(a). The calculated HHG spectra for H_2^+ in Figs. 2(a)-(d), respectively, show that the peak positions match well with those predicted by the selection rules and specified above. The spectrum displays circularly polarized harmonics up to the 80th harmonic order (H80). The ionization threshold (I_p) for the initially occupied $1\sigma_g$ molecular orbital is marked with the green dashed vertical line at ∼H19 ($19.13\omega_0$). Figure 2(b) shows the below- and near-threshold region (H1-H26). As one can see, the spectrum exhibits a clear doublet structure with the spacing between the main peaks equal to $3\omega_0$ and subpeak separation of ω_0. According to the general considerations discussed above, the components of the doublet (subpeaks within each main peak) must have circular polarization opposite to each other. Figures 2(c) and (d) show the above-threshold circularly polarized harmonics up to H80. In Fig. 2(c), starting at the doublet peak H49/H50, the contributions $S_x(\omega)$ and $S_y(\omega)$ to the total HHG spectrum from the x and y projections of the dipole acceleration are not well overlapped near the peak positions in the frequency domain, thus causing broadening of the peaks and deviation from perfect circular polarization. In Figs. 2(c) and (d), we see this phenomenon occurs for the doublets lying higher than H49/H50 in the plateau and near cutoff regions.

The generation of high-order harmonics by bichromatic counter-rotating circularly polarized laser fields results in harmonic doublets, where in each doublet the harmonics are circularly polarized with opposite handedness. However, this argument assumes that the driving-field frequency components are perfectly monochromatic. In reality, the laser pulse has a finite duration, hence the harmonic peaks have a finite width, and polarization may even vary even on the frequency range corresponding to the same harmonic peak. Also, our recent studies [15, 16] show that near-resonant radiation from excited states may also alter the polarization properties of the HHG spectrum in the below-threshold region. Here, we calculate the polarization properties of the harmonic radiation explicitly from the dipole acceleration data and show to what extent the harmonic peaks within the same doublet possess circular polarization with left and right handedness.

Suppose we have a monochromatic field with the components along x and y:

$$\begin{aligned} F_x &= a\cos(\omega t), \\ F_y &= b\cos(\omega t + \beta). \end{aligned} \tag{25}$$

Generally, the field amplitudes along x and y are different (with their ratio $r_{yx} = b/a$), and there is a phase shift β between the field oscillations in x and y directions. Actually, Eq. (25) represents an elliptically polarized field; the orientation of the ellipse in the $x - y$ plane depends on the parameters r_{yx} and β. The angle α which determines the orientation of one of the ellipse axes with respect to the x-axis is calculated as:

$$\alpha = -\frac{1}{2}\arctan\left(\frac{r_{yx}^2\sin(2\beta)}{1 + r_{yx}^2\cos(2\beta)}\right). \tag{26}$$

The second axis has the orientation angle $\alpha + \pi/2$. Assuming the first axis to be the major axis of the ellipse, the ellipticity parameter is calculated as follows:

$$\epsilon = \sqrt{\frac{\sin^2\alpha + r_{yx}^2\sin^2(\alpha+\beta)}{\cos^2\alpha + r_{yx}^2\cos^2(\alpha+\beta)}} \tag{27}$$

If the calculated ellipticity parameter ϵ appears greater than unity, then the first axis is actually the minor axis, and the ellipticity parameter is given by $1/\epsilon$. From the Fourier transform of the induced dipole acceleration (which represents the harmonic field), one can obtain the parameters r_{yx} and β and calculate the ellipticity for the specific frequency ω. The circular polarization ($\epsilon = 1$) is only possible if $\beta = \pm\pi/2$ and $r_{yx} = 1$.

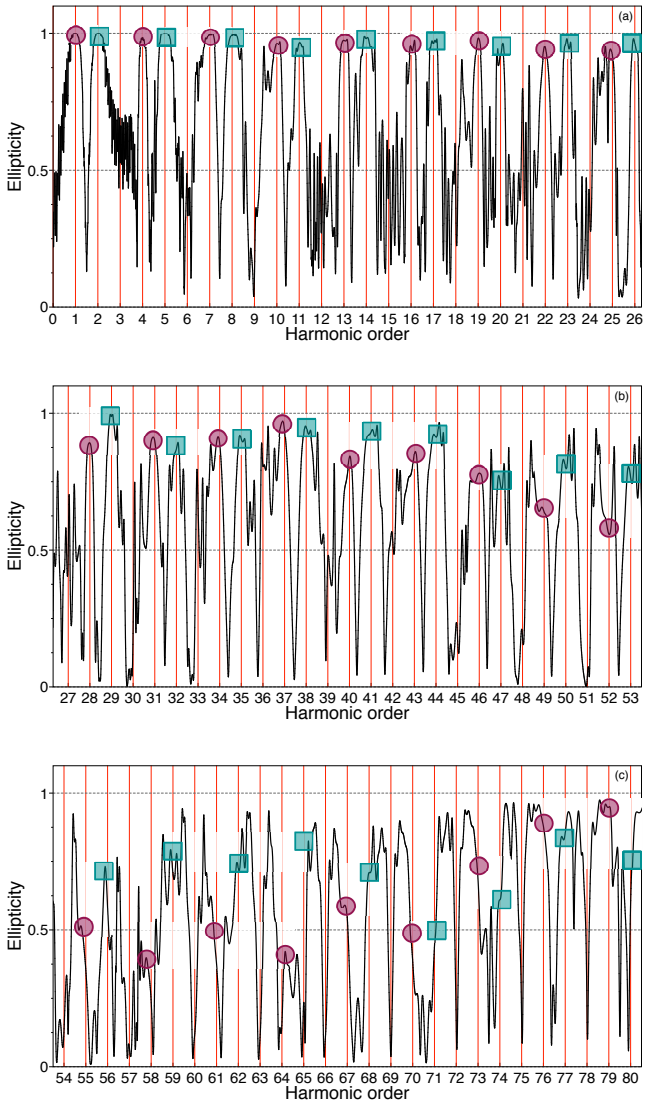

FIG. 3. (Color online) Ellipticity of the harmonic radiation from H_2^+ as a function of the harmonic order: (a) below- and near-threshold region (H1-H26), (b) above-threshold plateau region (H27-H53), and (c) above-threshold plateau and near cutoff region (H54-H80). The sine-squared laser pulse parameters used are the same as those in Figs. 1(a) and 2. The filled maroon circles and filled teal squares mark the peak positions of the harmonics $(3n_c + 1)\omega_0$ and $(3n_c + 2)\omega_0$, respectively, within each doublet.

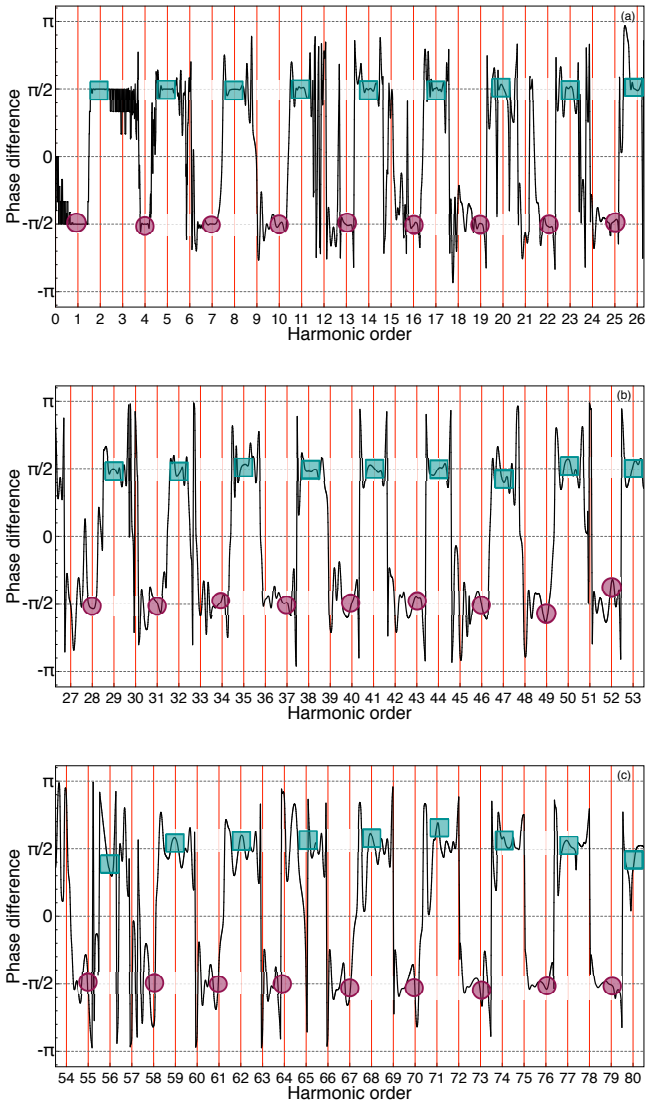

FIG. 4. (Color online) Phase shift between the x and y components of the harmonic field from H_2^+ as a function of the harmonic order: (a) below- and near-threshold region (H1-H26), (b) above-threshold plateau region (H27-H53), and (c) above-threshold plateau and near cutoff region (H54-H80). The sine-squared laser pulse parameters used are the same as those in Figs. 1(a) and 2. The filled maroon circles and filled teal squares mark the peak positions of the harmonics $(3n_c+1)\omega_0$ and $(3n_c+2)\omega_0$, respectively, within each doublet.

In Figs. 3 (ellipticity) and 4 (phase shift), the filled maroon circles and filled teal squares indicate the positions of harmonic peaks within each doublet [$(3n_c + 1)\omega_0$ and $(3n_c + 2)\omega_0$, respectively]. The circular polarization of the harmonics marked with the teal squares has the same handedness (right-helicity) as that of the driving field $\boldsymbol{E}_2(t)$, and the harmonics marked with the maroon circles are polarized with the same handedness (left-helicity) as the driving field $\boldsymbol{E}_1(t)$ for the sine-squared pulse (14) shown in Fig. 1(a).

Figures 3(a) and 4(a) show the ellipticity and phase shift, respectively, of the below- and near-threshold harmonics in the HHG spectrum of the H_2^+ molecule (Fig. 2). As one can see, for the below- and near-threshold harmonics, the ellipticity [Fig. 3(a)] is near unity and the phases [Fig. 4(a)] are very close to $\pm\pi/2$, indicating circular polarizations with left and right handedness. In Figs. 3(b) and 4(b), for the above-threshold harmonics in the plateau region, the ellipticity and phases start to deviate from perfect circular polarization. As we mentioned

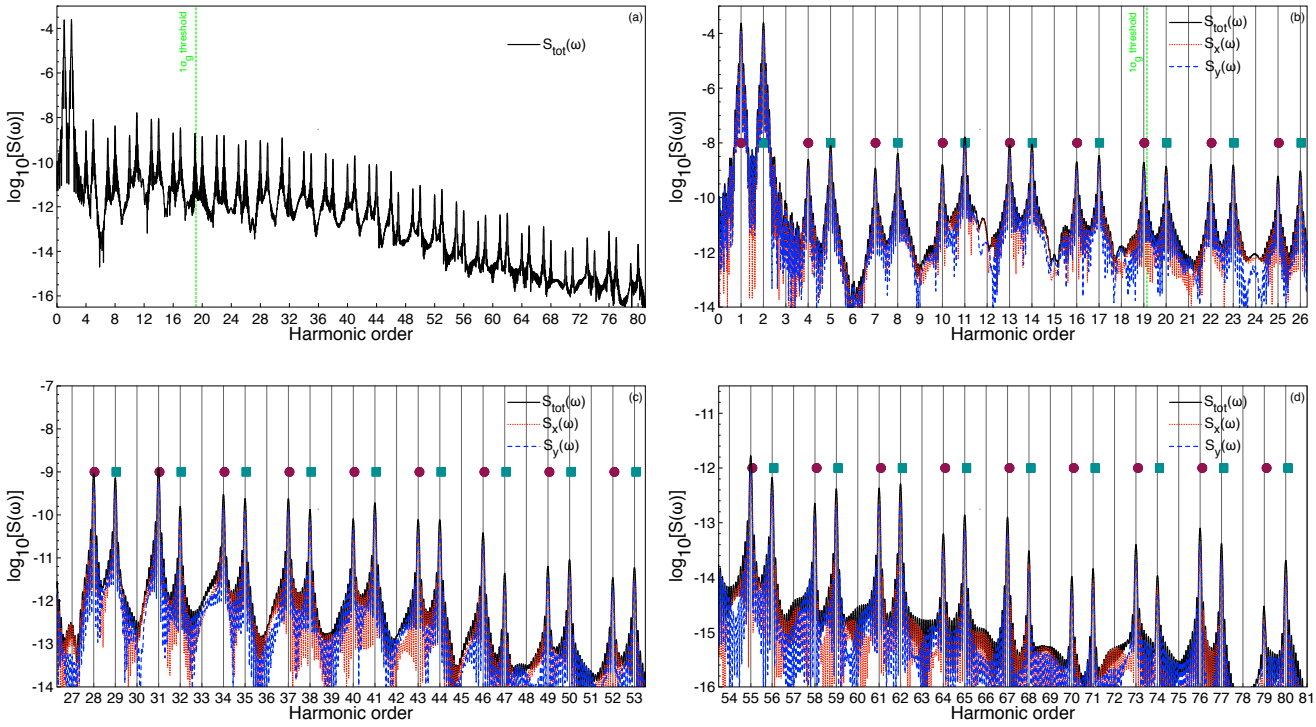

FIG. 5. (Color online) HHG spectrum $S_{\rm tot}(\omega)$ as well as contributions $S_x(\omega)$ and $S_y(\omega)$ from the x and y projections of the dipole acceleration for the H_2^+ molecule subject to the counter-rotating circularly polarized trapezoidal laser pulses. Circularly polarized harmonic doublets (a) up to ∼H80, (b) in the below- and near-threshold region (H1-H26), (c) in the above-threshold plateau region (H27-H53), and (d) in the above-threshold plateau and near cutoff region (H54-H80). The laser pulses have a time duration of 17 optical cycles (∼ 45 fs) of frequency ω_0 (wavelength 790 nm) and 34 optical cycles (∼ 45 fs) of frequency $2\omega_0$ (wavelength 395 nm). The black solid, red dotted, and blue dashed lines represent the HHG spectrum in the $S_{\rm tot}(\omega)$, $S_x(\omega)$, and $S_y(\omega)$ domains, respectively. The green vertical dashed line indicates the corresponding ionization threshold (I_p) of the $1\sigma_g$ molecular orbital (H19.13). Filled maroon circles and filled teal squares indicate the positions of the peaks with the frequencies $(3n_c+1)\omega_0$ and $(3n_c+2)\omega_0$, respectively. The separation between the peaks within each doublet is ω_0, and different doublets are separated by $3\omega_0$. Both bichromatic frequency components have the same peak field strength corresponding to the intensity of 2×10^{14} W/cm^2.

above when discussing Figs. 2(c) and (d), starting at the doublet peak H49/H50, the $S_x(\omega)$ and $S_y(\omega)$ contributions to the total HHG spectrum are not well overlapped for the frequencies corresponding to the peak positions. This reflects alterations in the ellipticity and phase for the harmonics higher than H49/H50, eventually resulting in substantial deviation of the generated harmonics from perfect circular polarization in the above-threshold plateau [Figs. 3(b) and 4(b)] and near cutoff [Figs. 3(c) and 4(c)] regions.

In Figs. 5(a)-(d), we present the HHG spectrum of H_2^+ for the trapezoidal (15) driving laser pulse shown in Fig. 1(b). The calculated harmonic peak positions match well with those predicted by the selection rules and specified above. The spectrum in Fig. 5(a) displays circularly polarized harmonics up to the 80th harmonic order (H80). The ionization threshold (I_p) for the initially occupied $1\sigma_g$ molecular orbital is marked with the green dashed vertical line at ∼H19 ($19.13\omega_0$). Figure 5(b) shows the below- and near-threshold region (H1-H26). As one can see, the spectrum exhibits a clear doublet structure with the spacing between the main peaks equal to $3\omega_0$ and subpeak separation of ω_0. Figures 5(c) and (d) show the above-threshold plateau and near-cutoff regions, respectively. The trapezoidal driving laser pulse [Fig. 1(b)] is more monochromatic (spectral width is narrower) than the sine-squared laser pulse [Fig. 1(a)]. Consequently, the harmonic peaks in Figs. 5(a)-(d) are narrower (and higher by 1-2 orders of magnitude) than those for the sine-squared pulse in Figs. 2(a)-(d). The contributions to the total HHG signal from the x and y projections of the dipole acceleration are well overlapped around the peak positions in Figs. 5(b)-(d), and this is a necessary condition for the perfect circular polarization of the generated harmonics. Strictly speaking, the selection rules discussed above are applied to perfectly monochromatic counter-rotating fields with the frequencies ω_0 and $2\omega_0$. The trapezoidal pulse shape (15) provides a better approximation of the monochromatic field than the sine-squared shape (14). This is the reason the

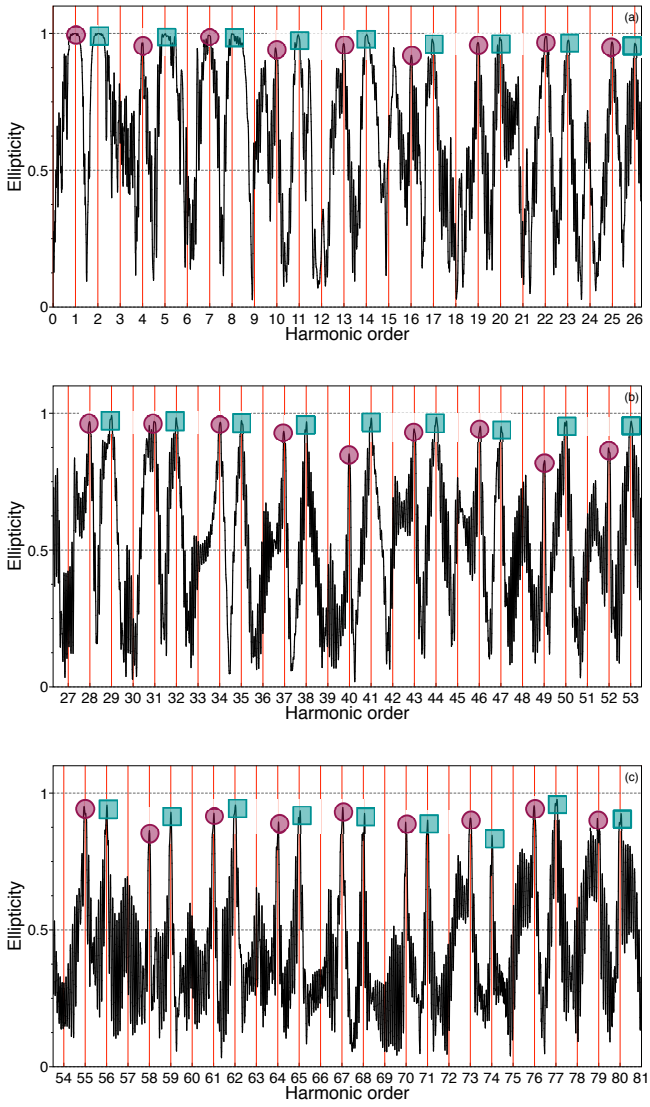

FIG. 6. (Color online) Ellipticity of the harmonic radiation from H_2^+ as a function of the harmonic order: (a) below- and near-threshold region (H1-H26), (b) above-threshold plateau region (H27-H53), and (c) above-threshold plateau and near cutoff region (H54-H80). The trapezoidal laser pulse parameters used are the same as those in Figs. 1(b) and 5. The filled maroon circles and filled teal squares mark the peak positions of the harmonics $(3n_c + 1)\omega_0$ and $(3n_c + 2)\omega_0$, respectively, within each doublet.

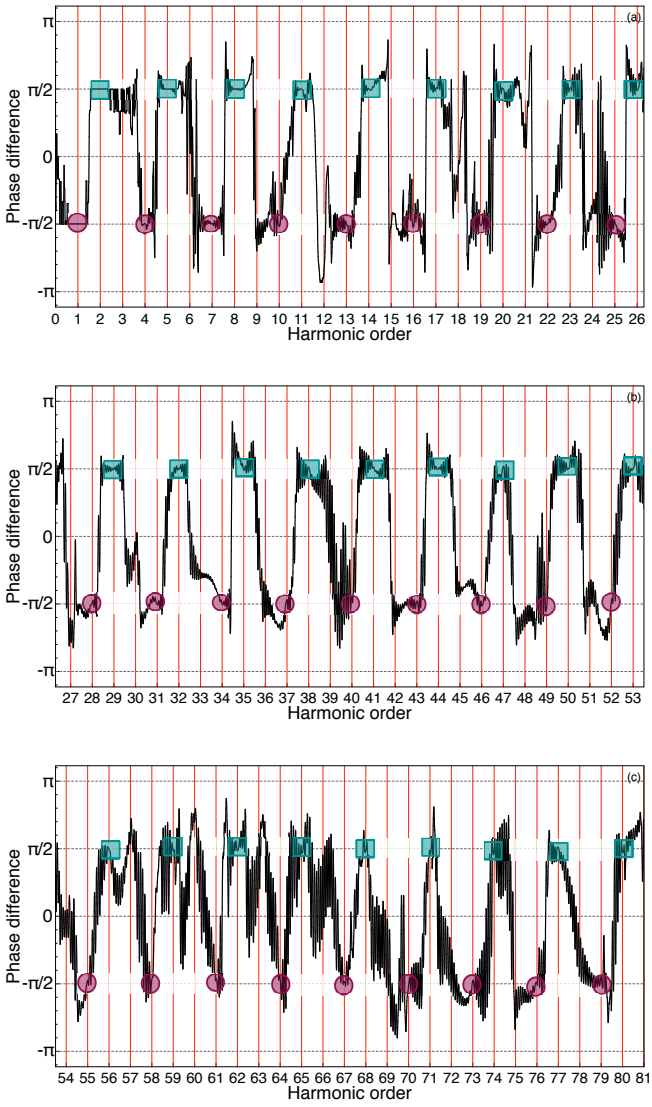

FIG. 7. (Color online) Phase shift between the x and y components of the harmonic field from H_2^+ as a function of the harmonic order: (a) below- and near-threshold region (H1-H26), (b) above-threshold plateau region (H27-H53), and (c) above-threshold plateau and near cutoff region (H54-H80). The trapezoidal laser pulse parameters used are the same as those in Figs. 1(b) and 5. The filled maroon circles and filled teal squares mark the peak positions of the harmonics $(3n_c+1)\omega_0$ and $(3n_c+2)\omega_0$, respectively, within each doublet.

sine-squared driving laser pulse does not show the perfect circular polarization predicted by the theory but the trapezoidal pulse gives rise to perfect circular polarization throughout the entire photon energy range of the calculated HHG spectrum. To prove quantitatively, next we will calculate the ellipticity (27) and phase shift of the harmonics shown in Figs. 5(a)-(d).

Figures 6 and 7 show the ellipticity and phase shift between the x and y components of the radiation field, respectively, for the harmonics in the HHG spectrum of Fig. 5. As one can see, for the below-, near-, and above-threshold harmonics, the ellipticity [Fig. 6(a-c)] is near unity and the phases [Fig. 7(a-c)] are very close to $\pm\pi/2$, indicating perfect circular polarizations with left and right handedness throughout the HHG spectrum ($\leq$ H80). The trapezoidal laser pulse shape (15) reveals better results for a perfectly circular polarized HHG spectrum, compared to the sine-squared laser pulse shape (14).

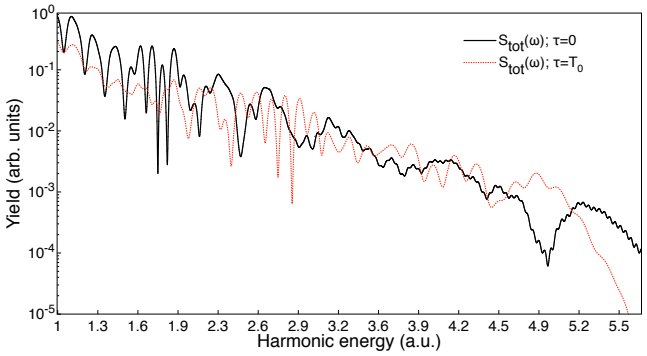

FIG. 8. (Color online) HHG spectrum $S(\omega)$ of the hydrogen atom subject to the counter-rotating few-cycle circularly polarized sine-squared laser pulses. The pulse durations measured in optical cycles of the frequency ω_0 are $N_1 = 3$ and $N_2 = 2$ for the ω_0 and $2\omega_0$ fields, respectively. Both bichromatic frequency components have the same peak intensity 1×10^{14} W/cm^2. The harmonic photon energy range shown is 1 to 5.5 a.u. Solid (black) line: $\tau = 0$ (zero time delay), dashed (red) line: $\tau = T_0$ (positive time delay (Eq. 13) corresponds to the $2\omega_0$ field arriving first.)

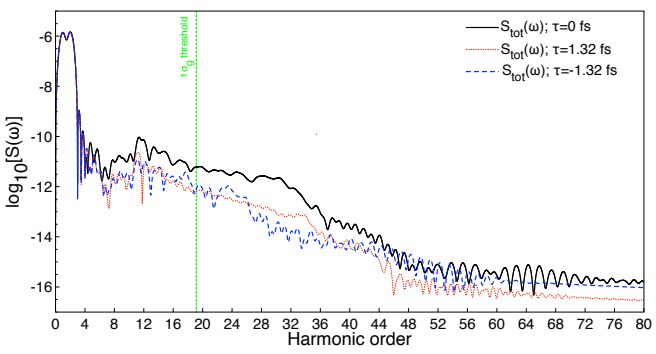

FIG. 9. (Color online) HHG spectrum $S(\omega)$ of the H_2^+ molecule subject to the counter-rotating few-cycle circularly polarized sine-squared laser pulses. The pulse duration is 2 optical cycles of the frequency ω_0 and peak intensity is 2×10^{14} W/cm^2 for both bichromatic components. Solid (black) line: $\tau = 0$ (zero time delay), dotted (red) line: $\tau = 1.32$ fs (positive time delay corresponds to the $2\omega_0$ field arriving first), and dashed (blue) line: $\tau = -1.32$ fs (negative time delay corresponds to the ω_0 field arriving first). The green vertical dashed line indicates the ionization threshold (I_p) of the $1\sigma_g$ molecular orbital.

IV. TIME DELAYED COUNTER-ROTATING FEW-CYCLE DRIVING LASER PULSES APPLIED TO H_2^+ MOLECULES

Here, we will investigate HHG by time-delayed few-cycle counter-rotating sine-squared laser pulses (14) first applied to atoms (H), and then to molecules (H_2^+). In both cases, we obtain the accurate wave functions by solving the full-dimensional time-dependent Schrödinger equation (TDSE), as described above in Sec. II (for the H atom case, the electric charge Z_2 is set to zero in Eq. (4)). In the calculations for the hydrogen atom, we adopt the carrier wavelengths 1600 nm (ω_0=0.0285 a.u.=0.78 eV) and 800 nm ($2\omega_0$=0.0570 a.u.=1.56 eV) and the pulse durations $T_{1,2} = 2\pi N_{1,2}/\omega_0$ where $N_1 = 3$ and $N_2 = 2$ for the 1600 nm and 800 nm fields, respectively. The peak intensities for both fields are equal to 1×10^{14} W/cm^2. All these parameters are the same as used in a recent theoretical investigation of the model hydrogen atom [36], except our pulse shape is sine-squared while the Gaussian pulse shape is used in Ref. [36].

Figure 8 shows the HHG spectrum of the H atom for the sine-squared (14) driving laser pulse with a zero time delay ($\tau = 0$) and a one-optical cycle time delay ($\tau = T_0$, where $T_0 = 2\pi/\omega_0$) on the harmonic photon energy range 1 to 5.5 a.u. A positive time delay (Eq. 13) corresponds to the $2\omega_0$ field arriving first. In Fig. 8, the solid (black) line is for a zero time delay, and the dashed (red) line corresponds to a time delay of $\tau = T_0$. As one can see, throughout the energy range $1-2.3$ a.u. where the HHG signal is the strongest, the zero time delay between the pulses delivers the largest harmonic yield. In this respect, our results are different from those of Ref. [36] where the harmonic yield is enhanced when a time delay is introduced, compared to the zero time delay case. For few-cycle laser pulses, however, the results strongly depend on the pulse envelope, thus a direct comparison between our results and those of Ref. [36] would be incorrect since different pulse shapes are used.

For our second case, we investigate HHG by the H_2^+ molecule subject to the time-delayed few-cycle counter-rotating sine-squared laser pulses (14). Here, we will make use of the carrier wavelengths 790 and 395 nm and peak intensity 2×10^{14} W/cm^2 for both fields, as shown in Figs. 1(a) and 2. We choose the same pulse duration of $T = 4\pi/\omega_0$ for both bichromatic components, that is 2 optical cycles of the field with the wavelength 790 nm and 4 optical cycles of the field with the wavelength 395 nm. One cycle of the ω_0 and $2\omega_0$ fields has a duration of 2.64 and 1.32 fs, respectively. In Fig. 9, we present the HHG spectra of the H_2^+ molecule for the time delays $\tau = 0$, ±1.32 fs [Eqs. (12) and (13)]. Positive (negative) time delays (Eq. 13) correspond to the $2\omega_0$ (ω_0) field arriving first. In Fig. 9, the solid (black) line, dotted (red) line, and dashed (blue) line have time delays $\tau = 0$, $\tau = 1.32$ fs, and $\tau = -1.32$ fs, respectively. The spectrum displays circularly polarized harmonics up to the 80th harmonic order (H80). The ionization threshold (I_p) for the initially occupied $1\sigma_g$ molecular orbital is marked with the green dashed vertical line at ∼H19 ($19.13\omega_0$). Figure 9 clearly displays a zero time delay ($\tau = 0$, solid (black) line) has the largest HHG intensity throughout the spectrum, except for harmonic orders H47–H52, where the negative time delay ($\tau = -1.32$ fs, dashed (blue) line) has the greater HHG intensity. Such results are actually understandable. A circularly polarized pulse alone cannot generate high-order harmonics because of the angular

momentum conservation; one needs two counter-rotating pulses for this process (see discussion at the beginning of Sec. III). Obviously, the highest harmonic yield can be achieved when the overlap area of the two pulses in the time domain contains their peak intensity regions. For the symmetric pulses studied here, it corresponds to the zero time delay between the pulses.

We have also investigated several longer pulse durations ($T = 6\pi/\omega_0$, $T = 10\pi/\omega_0$, and $T = 34\pi/\omega_0$) for counter-rotating sine-squared laser pulses (14) with different time delays applied (not shown here). We conclude that for longer pulses there are no distinct differences in the HHG intensities between the zero and non-zero time delays in the range $\tau = \pm 1.37... \pm 4.11$ fs.

V. CONCLUSION

In this paper, we have presented a detailed investigation and analysis of H_2^+ diatomic molecules and H atoms subject to bichromatic counter-rotating circularly polarized intense laser fields. The generated high-order harmonic spectrum exhibits a doublet structure where the harmonics within the same doublet have opposite (left and right) circular polarizations.

We found that qualitatively different nonlinear optical responses and dynamics are predicted for bichromatic counter-rotating sine-squared and trapezoidal pulse shapes. First, the sine-squared pulse, because of its larger bandwidth in the frequency domain, does not produce perfect circularly polarized harmonics. At the same time, the trapezoidal pulse provides a better approximation of the monochromatic field than the sine-squared pulse and produces perfect circularly polarized harmonics. Second, the contributions to the total HHG signal from the x and y projections of the dipole acceleration are well overlapped around the peak positions when the trapezoidal pulse shape is used; this is not the case for the sine-squared pulse. We also note that the harmonic peaks generated by the trapezoidal pulse are much narrower in the frequency domain and 1-2 orders of magnitude higher compared to the harmonics generated by the sine-squared pulse while the emitted radiation energies are comparable.

We have also investigated the effect of the time delay between the ω_0 and $2\omega_0$ components of the driving laser pulse on HHG by H atoms and H_2^+ molecules. Our full-dimensional calculations for the hydrogen atom reveal that the zero time delay between the ω_0 and $2\omega_0$ components delivers the largest harmonic yield. This observation is intuitively understandable because isolated circularly polarized pulses cannot generate high-order harmonics due to the angular momentum conservation, even if we have two such pulses with counter-rotating polarization vectors but separated by a substantial time interval. One needs well overlapped counter-rotating pulses to generate harmonics, and the higher the intensity of the driving field in the overlap area, the larger harmonic yield can be expected.

In the study of the time delay effect on HHG by H_2^+ molecules, we have performed calculations for several short and long pulse durations. The results generally confirm our findings for the hydrogen atom. When considering short pulses ($< T = 6\pi/\omega_0$), the zero time delay corresponds to the highest HHG intensity. For longer pulses ($> T = 6\pi/\omega_0$), we find no visible effect of the time delay and no distinct differences in the HHG intensities between the cases of the zero and non-zero time delays, if the latter do not exceed two optical cycles of the fundamental frequency. Our findings can help to determine appropriate conditions for perfect circular polarization of the generated harmonics which can be applied to advanced studies of chiral-sensitive light-matter interactions such as circular dichroism, ultrafast magnetization and spin dynamics in the future.

ACKNOWLEDGMENTS

This work was partially supported by the Chemical Sciences, Geosciences and Biosciences Division of the Office of Basic Energy Sciences, Office of Sciences, U. S. Department of Energy under grant No. DE-FG02-04ER15504. We also acknowledge the partial support of the Ministry of Science and Technology of Taiwan and National Taiwan University (Grants No. 106R104021 and 106R891701).

[1] T. Fan, P. Grychtol, R. Knut, C. Hernandez-Garcia, D. D. Hickstein, D. Zusin, C. Gentry, F. J. Dollar, C. A. Mancuso, C. W. Hogle, et al., Proc. Natl. Acad. Sci. U.S.A. **112**, 14206 (2015).

[2] M. Chini, X. Wang, Y. Cheng, H. Wang, Y. Wu, E. Cunningham, P.-C. Li, J. Heslar, D. Telnov, S. Chu, et al., Nat. Photonics **8**, 437 (2014).

[3] I.-Y. Park, S. Kim, J. Choi, D.-H. Lee, Y.-J. Kim, M. Kling, M. Stockman, and S.-W. Kim, Nat. Photonics **5**, 677 (2011).

[4] S. Kim, J. Jin, Y.-J. Kim, I.-Y. Park, K. Seung-Woo, and S.-W. Kim, Nature **453**, 757 (2008).

[5] J. Heslar, D. A. Telnov, and S. I. Chu, Phys. Rev. A **93**, 063401 (2016).

[6] A. Rundquist, C. G. Durfee, Z. Chang, C. Herne, S. Backus, M. M. Murnane, and H. C. Kapteyn, Science **280**, 1412 (1998).

[7] A. Fleischer, O. Kfir, T. Diskin, P. Sidorenko, and O. Cohen, Nat. Photonics **8**, 543 (2014).

[8] O. Kfir, P. Grychtol, E. Turgut, R. Knut, D. Zusin, A. Fleischer, E. Bordo, T. Fan, D. Popmintchev, T. Popmintchev, et al., J. Phys. B **49**, 123501 (2016).

[9] E. Turgut, C. La-o vorakiat, J. M. Shaw, P. Grychtol, H. T. Nembach, D. Rudolf, R. Adam, M. Aeschlimann, C. M. Schneider, T. J. Silva, et al., Phys. Rev. Lett. **110**, 197201 (2013).

[10] S. Mathias, C. La-O-Vorakiat, P. Grychtol, P. Granitzka, E. Turgut, J. M. Shaw, R. Adam, H. T. Nembach, M. E. Siemens, S. Eich, et al., Proc. Natl. Acad. Sci. U.S.A. **109**, 4792 (2012).

[11] C. La-O-Vorakiat, M. Siemens, M. M. Murnane, H. C. Kapteyn, S. Mathias, M. Aeschlimann, P. Grychtol, R. Adam, C. M. Schneider, J. M. Shaw, et al., Phys. Rev. Lett. **103**, 257402 (2009).

[12] O. Kfir, P. Grychtol, E. Turgut, R. Knut, D. Zusin, D. Popmintchev, T. Popmintchev, H. Nembach, J. M. Shaw, A. Fleischer, et al., Nat. Photonics **9**, 99 (2015).

[13] D. B. Milošević, J. Phys. B **48**, 171001 (2015).

[14] L. Barreau, K. Veyrinas, V. Gruson, S. J. Weber, T. Auguste, J.-F. Hergott, F. Lepetit, B. Carré, J.-C. Houver, D. Dowek, et al., Nat. Commun. **9**, 4727 (2018).

[15] J. Heslar, D. A. Telnov, and S. I. Chu, Phys. Rev. A **96**, 063404 (2017).

[16] J. Heslar, D. A. Telnov, and S. I. Chu, Phys. Rev. A **97**, 043419 (2018).

[17] S. Long, W. Becker, and J. K. McIver, Phys. Rev. A **52**, 2262 (1995).

[18] H. Eichmann, A. Egbert, S. Nolte, C. Momma, B. Wellegehausen, W. Becker, S. Long, and J. K. McIver, Phys. Rev. A **51**, R3414 (1995).

[19] G. Dixit, A. Jiménez-Galán, L. Medišauskas, and M. Ivanov, Phys. Rev. A **98**, 053402 (2018).

[20] A. Ferré, C. Handschin, M. Dumergue, F. Burgy, A. Comby, D. Descamps, B. Fabre, G. A. Garcia, R. Géneaux, L. Merceron, et al., Nat. Photonics **9**, 93 (2014).

[21] C. Chen, Z. Tao, C. Hernández-García, P. Matyba, A. Carr, R. Knut, O. Kfir, D. Zusin, C. Gentry, P. Grychtol, et al., Science Advances **2**, e1501333 (2016).

[22] G. Lambert, B. Vodungbo, J. Gautier, B. Mahieu, V. Malka, S. Sebban, P. Zeitoun, J. Luning, J. Perron, A. Andreev, et al., Nat. Commun. **6**, 6167 (2015).

[23] P.-C. Huang, C. Hernández-García, J.-T. Huang, P.-Y. Huang, C.-H. Lu, L. Rego, D. D. Hickstein, J. L. Ellis, A. Jaron-Becker, A. Becker, et al., Nat. Photonics **12**, 349 (2018).

[24] K. M. Dorney, J. L. Ellis, C. Hernández-García, D. D. Hickstein, C. A. Mancuso, N. Brooks, T. Fan, G. Fan, D. Zusin, C. Gentry, et al., Phys. Rev. Lett. **119**, 063201 (2017).

[25] M. Abramowitz and I. Stegun, eds., *Handbook of Mathematical Functions* (Dover, New York, 1965).

[26] D. A. Telnov and S. I. Chu, Phys. Rev. A **80**, 043412 (2009).

[27] D. A. Telnov, J. Heslar, and S. I. Chu, Phys. Rev. A **95**, 043425 (2017).

[28] J. Heslar and S. I. Chu, Sci. Rep. **6**, 37774 (2016).

[29] K. N. Avanaki, D. A. Telnov, and S. I. Chu, J. Phys. B **49**, 114002 (2016).

[30] S. K. Son, D. A. Telnov, and S. I. Chu, Phys. Rev. A **82**, 043829 (2010).

[31] D. A. Telnov and S. I. Chu, Phys. Rev. A **76**, 043412 (2007).

[32] X. M. Tong and S. I. Chu, Chem. Phys. **217**, 119 (1997).

[33] E. Pisanty, S. Sukiasyan, and M. Ivanov, Phys. Rev. A **90**, 043829 (2014).

[34] D. B. Milošević, Phys. Rev. A **92**, 043827 (2015).

[35] E. Hasović, S. Odžak, W. Becker, and D. B. Milošević, Mol. Phys. **115**, 1750 (2017).

[36] M. V. Frolov, N. L. Manakov, A. A. Minina, N. V. Vvedenskii, A. A. Silaev, M. Y. Ivanov, and A. F. Starace, Phys. Rev. Lett. **120**, 263203 (2018).